Geophysical Research Letters

RESEARCH LETTER
10.1029/2023GL106376

Mesoscale Meridional Heat Transport Inferred From Sea Surface Observations

Yanxu Chen[1] and Lisan Yu[1]

[1]Department of Physical Oceanography, Woods Hole Oceanographic Institution, Woods Hole, MA, USA

Key Points:

- The geostrophic component of meridional heat transport (MHT) at the mesoscale is 10 times larger than the Ekman component
- SSH-SST coherent eddies dominate the spatial patterns of MHT at the mesoscale
- Though incomparable in magnitude with the large scale MHT, mesoscale eddies can still transport 30 TW of heat near sea surface

Supporting Information:

Supporting Information may be found in the online version of this article.

Correspondence to:

Y. Chen,
yanxu.chen@whoi.edu

Citation:

Chen, Y., & Yu, L. (2024). Mesoscale meridional heat transport inferred from sea surface observations. *Geophysical Research Letters*, *51*, e2023GL106376. https://doi.org/10.1029/2023GL106376

Received 20 OCT 2023
Accepted 16 FEB 2024

Author Contributions:

Conceptualization: Yanxu Chen, Lisan Yu
Funding acquisition: Lisan Yu
Investigation: Yanxu Chen, Lisan Yu
Methodology: Yanxu Chen, Lisan Yu
Resources: Lisan Yu
Supervision: Lisan Yu
Validation: Yanxu Chen, Lisan Yu
Visualization: Yanxu Chen
Writing – original draft: Yanxu Chen
Writing – review & editing: Lisan Yu

Abstract The ocean regulates the Earth's climate by transporting heat from the equator to the poles. Here, we use satellite-based sea surface observations of air-sea heat fluxes and eddy detection to investigate the mesoscale heat transport. "Mesoscale" refers to both the Eulerian perspective as the spatio-temporal scales of ∼100 km and ∼1 month, as well as the Lagrangian aspect as isolated vortices identified from the dynamic topography. Paradoxically, there are a considerable number of mesoscale eddies inconsistent between their surface thermal and dynamic signals, that is, cold-core anticyclones and warm-core cyclones are globally prevalent. On account of such inconsistency, we show that the mesoscale meridional heat transport carried by geostrophic components is 10 times larger than (and opposite in direction to) that of the wind-driven Ekman components. An offset between SSH-SST coherent and incoherent eddies in the Ekman heat transport is apparent, whereas the geostrophic heat transport is contained within coherent eddies.

Plain Language Summary Rotating water masses in the ocean, termed as mesoscale eddies, are dynamically important features because they can transport nutrients and displace heat in the Earth's climate system. In the same manner as the atmospheric weather systems that are associated with high or low pressures, mesoscale eddies are accompanied by sea level anomalies and therefore can be observed by satellite images. Conventionally, anticyclonic eddies detected as clockwise vortices in the Northern Hemisphere display warm temperature anomalies at the center. However, recent studies have found that the sea surface temperature signal of an eddy might be uncertain and even contradictory to their dynamical circulation patterns. In this study, we combine sea surface observations of temperature and velocity fields to determine the patterns of global ocean heat transport associated with mesoscale eddies.

1. Introduction

In the current Earth's climate system, more than 90% of the total human-induced energy imbalance accumulates in the ocean as increased ocean heat content (OHC) (Cooley et al., 2022). Such rapid anthropogenic warming over the past few decades has contributed to significant sea level rise (Zickfeld et al., 2017), intensified rainfalls (Madakumbura et al., 2021), severe deoxygenation (Keeling et al., 2010) and declines in ice sheets and glaciers in the polar regions (Marzeion et al., 2014). Traditionally speaking, a combination of shallow wind-driven gyres at the subtropics and deep circulations at high latitudes regulates the large-scale OHC patterns by redistributing water masses (Ferrari & Ferreira, 2011; Talley, 2003; Trenberth & Caron, 2001). From such perspective, heat, or temperature to be more specific, is an intrinsic characteristic of water masses and can be identified and traced from ventilation processes. Some studies, on the other hand, distinguished heat transport from temperature, for which the former represents thermal energy transfer with a mass conservation while the latter does not strictly constrain mass (Warren, 1999).

In previous studies, estimates of ocean heat transport (OHT) fall into one of three categories: (a) bulk formula deductions, (b) residual calculations, and (c) direct in situ full-depth measurements. The first two methods produce what are considered indirect OHT estimates, as they do not require water column observations but rather assess the energy budget linked to the atmosphere. In other words, assuming that there is no regional storage of heat within the ocean, air-sea heat fluxes computed globally are thus balanced by ocean heat divergence (described as the 3D method in Section 2). To be more specific, bulk formula of heat transfer are equations with empirical coefficients that are applied to observations of constituent variables at the air-sea interface, while residual calculations consider the energy difference between top of the atmosphere and meteorological measurements. By applying the latter, Trenberth and Fasullo (2017) have shown that the global average of large-scale meridional heat transport (MHT) approaches 2 PW as the maximum at 15°N in the direction toward the pole,

with the largest contribution from the Atlantic Ocean. Compared with this 3D perspective of heat conservation, direct in situ observations typically compute heat transport across 2D hydrographic sections, which commonly produce a narrower range of MHT estimates with lower uncertainties (Bryden et al., 1991; Johns et al., 2011; Roemmich & Wunsch, 1985).

Although the partitioning of large-scale OHT among different basins has been systematically quantified, it is still difficult to determine such transport at the meso or even smaller scales from either observations or numerical models. This difficulty is in part due to the vague definition of the "mesoscale," since some studies considered it to be the transient component apart from a longer-term average (Delman & Lee, 2021) while other studies track coherent eddying structures in a Lagrangian perspective (Bashmachnikov et al., 2023; Chelton et al., 2011; B. Sun et al., 2019). Recent observations of the inconsistency between sea surface temperature (SST) and sea surface height (SSH) anomalies in defining eddies alternatively demonstrate the issue. In the traditional context, anti-cyclonic eddies detected as positive SSHAs typically enclose a distinct warm temperature anomaly at the center and thus are capable of warming the marine boundary layer. However, recent observations have shown that about 20% of eddies detected from altimeter data exhibit unconventional characteristics, such as warm-core cyclones (CEs) and cold-core anticyclones (AEs) (Itoh & Yasuda, 2010; Ni et al., 2021; Moschos et al., 2022; W. Sun et al., 2022), which do not conform to the standard definition of mesoscale eddies based on sea surface height and temperature coherence. We refer to these unconventional eddies as SSH-SST incoherent eddies hereafter. Generations of such counter-intuitive features at the mesoscale remain to be studied.

With the focus on how mesoscale eddies contribute to MHT in the context of both sea surface dynamic and thermodynamic measurements, the structure of the paper is organized as follows: Section 2 begins with a detailed presentation of heat transport dynamics in both 2D and 3D contexts, accompanied by descriptions of how each component in MHT is approached from two satellite-based data sets: the Objectively Analyzed Air-Sea Fluxes (OAFlux2) (Yu, 2019) and the Mesoscale Eddy Trajectories Atlas (META3.2 DT) (Pegliasco et al., 2022). In terms of logic, thermal and dynamical patterns obtained from OAFlux2 were first confined to the mesoscale by application of spatial and temporal windows. Subsequently, these anomalies were extracted for each META eddy detected by closed contours of absolute dynamic topography (ADT). Therefore, the term of "mesoscale" fields hereafter refer to anomalies from the large scale, while "mesoscale eddy" is always concerned with a dynamically detected vortex. In Section 3, the 20-year composite of global eddy-induced air-sea net heat fluxes is presented, followed by spatial patterns and long-term averages of MHT. A discussion on potential physical explanations is provided at last.

2. Mechanisms and Computations of Ocean Heat Budget

2.1. Ocean Heat Budget in 3D and 2D Contexts

Indirect estimates of OHT begin with the integration of the complex 3D oceanic and atmospheric circulations in density coordinates for obtaining a description of the overturning circulation (Czaja & Marshall, 2006; Nurser & Lee, 2004). If one considers the heat budget for ocean surface layer, the temporal evolution of temperature is given by the sum of net heat exchange with the atmosphere, advective heat transport by currents and some diffusive processes within this layer. For example,

$$\frac{\partial T}{\partial t} + u \cdot \nabla T = \left(K_v T_z\right)_z. \tag{1}$$

Here, K_v represents the diffusive coefficient over the surface layer, dependent on the vertical coordinate z. We could thus integrate Equation 1 over volume and consider the heat budget instead, which is

$$\int \rho C_p \left(\frac{\partial T}{\partial t} + u \cdot \nabla T\right) dV = \int \rho C_p \left(K_v T_z\right)_z dV \approx \iint \rho C_p \left(K_v T_z\right)\Big|_{bot}^{top} dx dy \approx \iint F_s \, dx dy, \tag{2}$$

where ρ represents seawater density, C_p the specific heat of water at constant pressure, F_s the net air-sea heat flux at the surface. This equation relates the temporal change of near-surface heat content to fluxes at the air-sea interface, while the heat transfer at the bottom of this layer is either assumed to be zero or neglected.

On the other hand, direct estimates of OHT are based on observations of water column temperature and velocity. The general expression for the computation of heat transport perpendicular to any 2D hydrographic transect is

$$OHT = \iint \rho C_p T v \, dx dz, \tag{3}$$

where v represents the velocity perpendicular to the transect. Typically, ρ and v are functions of temperature, salinity and pressure. However, v is sometimes computed as a geostrophic balance with corrections from ageostrophic motions like Ekman dynamics. The integral for Equation 3 is taken vertically and horizontally across the transect where a mass balance is satisfied for the ocean's large scale (Warren, 1999). As a result, estimates using Equation 3 are typically constructed from temperature, salinity, and pressure observations of hydrographic sections using a variety of techniques. A simplified version is to assume constant values of ρ, C_p and a uniform surface layer thickness h, of which the latter means the integrand of Tv is independent of depth. Equation 3 then becomes

$$OHT = \rho C_p h \int Tv \, dx. \tag{4}$$

This 2D version of OHT calculation depends on temperature and velocity variations along any hydrographic section, which has been widely used to study heat and salt transport at the mesoscale (Hausmann & Czaja, 2012; Melnichenko et al., 2017).

Based on Equation 4, in this study we further separate velocity v associated with any nearly-geostrophic eddy into 2 components: the geostrophic component which is simply the rotation of an eddy, and the Ekman component calculated from the wind stress. If all mesoscale eddies are SSH-SST coherent eddies with identical SSH and SST anomaly center locations, the geostrophic component of horizontal heat transport will result in a null effect. Therefore, it is the horizontal discrepancy between eddy's SSH and SST centers that leads to the geostrophic OHT at the mesoscale. Additionally, the Ekman velocity is directly derived from the satellite-observed wind fields with the consideration of eddy's relative vorticity (Gaube et al., 2015; Stern, 1965),

$$\boldsymbol{u}_{ek} = \frac{\boldsymbol{\tau}}{\rho(f+\zeta)H} \times \hat{k}. \tag{5}$$

Here, $\boldsymbol{\tau}$ indicates the surface wind stress, f and ζ the planetary and relative vorticities respectively. We also assume a constant Ekman layer thickness H to be 50 m in the calculation of OHT.

2.2. Combination of Air-Sea Dynamic and Thermal Observations

In this study, SST, wind speed and direction, turbulent heat flux, Ekman transport and other related sea surface variables are taken from OAFlux2, which is a new satellite-derived 0.25-degree gridded air-sea flux analysis (1988 to the present) developed under the auspices of NASA's Making Earth System Data Records for Use (MEaSUREs) program (Yu, 2019). The computation of turbulent heat flux is based on the version 3.6 of the Coupled Ocean-Atmosphere Response Experiment (COARE) bulk algorithm (Fairall et al., 2003). In OAFlux2, wind speed is synthesized from 18 satellite sensors including both microwave radiometers and scatterometers (Yu & Jin, 2014a, 2014b), and air humidity and temperature are retrieved from 13 satellite microwave sounders and radiometers (Yu & Jin, 2018). To estimate the net heat flux at the air-sea interface (i.e., the sum of radiation and turbulent flux), we also used the radiation data from the CERES SYN1deg product which were modeled from 1-hourly radiances and cloud property data (Doelling et al., 2016).

In terms of eddy tracking, the META data set was applied as the eddy atlas (Pegliasco et al., 2022), in which a novel SSH-based automatic identification algorithm was utilized to determine and track eddies through spatially high-pass filtered SSH-closed contours (Chelton et al., 2011). The date of eddy occurrence, location, radius, and amplitude are contained within this data set, but information regarding eddy contours is absent. The amplitude of the anticyclonic (cyclonic) eddy is defined as the absolute difference between the maximum (minimum) sea level anomaly (SLA) values within the eddy range and the average SLA value at the eddy's edge. In this study, the time period chosen for constructing eddy statistics and their correlation with air-sea variables is between 1999 and 2018 (i.e., 20 years in total). In an attempt to accurately evaluate the geostrophic velocity associated with the

META eddy detection, the same source of daily sea surface height and geostrophic velocity derivation is applied, provided by the E.U. Copernicus Marine Service Information (Copernicus Marine Service, 2023).

To associate all air-sea variables with eddy detection, our first step is to limit the SST, velocities and net air-sea heat flux signals to the ocean mesoscale. Following previous studies (Liu et al., 2020; Villas Bôas et al., 2015), a temporal band-pass Butterworth window is applied to preserve periods between 7 and 90 days, which correspond to the typical time scales of eddies. In the next step, a moving average Hann window is used to filter spatial scales larger than 600 km. Subsequently, these spatially-filtered maps containing signals with wavelengths longer than 600 km are subtracted from the time-filtered maps to construct the anomaly maps associated with mesoscale features. We next also define the large scale as the residual between the original distribution and the mesoscale anomalies.

After filtering out the irrelevant scales for air-sea variables, we composite spatial patterns of SST and heat fluxes inside all identified eddies together. For each identified eddy, the air-sea anomalies are interpolated onto a uniform high-resolution grid, normalized by the radial distance from the eddy center to the eddy edge. The spatial extent of the grid is chosen to represent the anomaly fields to a distance twice the eddy radius R in each direction. This scaling allows to average the anomaly of thousands of eddies as a single composite map, consisting of an efficient way to depict their mean signature on surface variables. The composite maps of eddy-induced anomalies are produced by averaging anomaly fields over all eddies selected by eddy types. In this study, we separate warm and cold eddies in terms of the extreme SST anomalies inside the eddy radius R. For example, warm-core eddies are determined if the extreme SST anomaly inside the eddy contour is positive. These two separations according to polarity and temperature lead to four eddy types: SSH-SST coherent eddies (warm AEs and cold CEs), and SSH-SST incoherent eddies (warm CEs and cold AEs).

3. Results: Meridional Heat Transport at the Mesoscale

In this section, composite maps of net air-sea heat fluxes for SSH-SST coherent and incoherent eddies will be presented first, followed by a quantification of MHT for each component representing the transport by the Ekman flow or geostrophic circulation associated with mesoscale eddies.

The averaged spatial distribution of net air-sea heat flux anomalies inside eddies is shown in Figure 1. These composite maps were obtained by averaging eddy-induced anomalies with radius larger than 30 km and amplitude larger than 35 mm, corresponding to approximately 2.26 million anticyclonic and 2.25 million cyclonic eddy realizations in the Northern Hemisphere, and 4.15 million anticyclonic and 4.36 million cyclonic eddies in the Southern Hemisphere. For AEs and CEs in both hemispheres, we further separate cold and warm eddies according to the extreme values of SST inside eddy's SSH contours. The percentage of warm and cold eddies for each row is displayed at the bottom right corner of every component. It is obvious that in both hemispheres, the features of SSH-SST coherent eddies dominate over incoherent eddies (as to compare the patterns of first and second columns in Figure 1). An analogous figure of SST to Figure 1 of air-sea flux shows very similar spatial structure and is thus neglected for a duplicate of plotting.

We also notice in Figure 1 of small distances between the SST- and SSH-determined eddy centers. This shift of heat anomaly from the SSH-based eddy core is mainly northwestward (southwestward) for Northern Hemisphere AEs (CEs) and Southern Hemisphere CEs (AEs). Such difference between the SST and SSH centers is also consistent with previous studies on SSH-SST coherent eddies that the westward displacement of SST is associated with the β-effect (Chassignet & Cushman-Roisin, 1991; Cushman-Roisin et al., 1990). In addition to the zonal movement, Morrow et al. (2004) considered meridional propagation of eddies and concluded that the divergence in eddy pathways for both hemispheres implies a net equatorward heat transport. Such concern with the migration speed of individual eddies is not considered here, and only the Ekman and geostrophic velocities are examined for a comparison in the context of MHT. Moreover, SSH-SST coherent eddies in the Southern Hemisphere display greater consistency between their dynamic and thermodynamic centers. This is in part due to a higher intensity of net heat flux inside coherent eddies as shown in (c2) and (d2), and in part ascribed to a larger number of coherent eddies compared with incoherent ones. However, we also observe a considerable number of SSH-SST incoherent eddies in Figure 1 (column 3), albeit less than their coherent counterparts. SSH-SST coherent and incoherent eddies are located symmetrically in terms of the eddy's SSH center. In the Northern Hemisphere, it is easy to identify cold AEs and warm CEs in the averaged patterns of AEs and CEs.

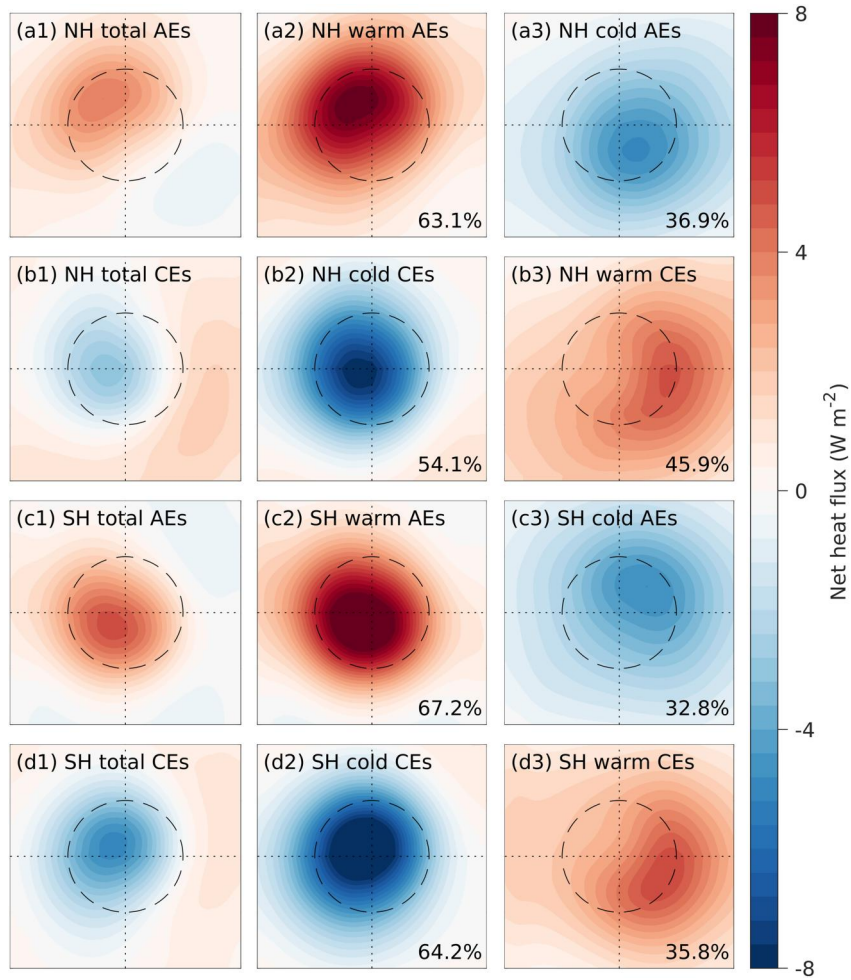

Figure 1. Composite maps of eddy-induced net air-sea heat flux. From top to bottom, each row is associated with the Northern Hemisphere (NH) anticyclones, cyclones, Southern Hemisphere (SH) anticyclones and cyclones. The total number of eddies is included in the text. For the second and third columns, the percentage of warm and cold components is shown at the bottom right corner. The axes in the composite maps are the normalized distance between the eddy center and twice the eddy edge. The circle of dashed lines in each map marks an eddy contour with the effective eddy radius.

Following the air-sea net heat flux pattern, Figure 2 illustrates the spatial distribution of eddy-induced MHT in terms of the Ekman and geostrophic components, as calculated separately by Equation 4. With regard to amplitudes, the geostrophic component at the mesoscale as shown in (a2), (b2), and (c2) is about 10 times larger than the Ekman component of (a1), (b1), and (c1). The total mesoscale signal of MHT in (a) can be divided into one constituent inside SSH-SST coherent eddies as in (b) and the other constituent outside coherent eddies as in (c). In terms of the total Ekman component, MHT inside coherent eddies shown in (b1) has a reversed and dominant spatial pattern compared with MHT outside coherent eddies displayed in (c1). The same comparison between (b2) and (c2) for the geostrophic component, however, indicates that the total amount of MHT is carried by SSH-SST coherent eddies, with the outside-eddy component appearing as small deviations. While the Ekman velocity associated with coherent eddies transports heat toward the equator as shown in (b1), the geostrophic components displayed in (b2) transfer heat toward the pole in both hemispheres. In other words, the Ekman component of MHT is opposite in direction to the geostrophic component, albeit 10 times smaller. Panels (d1) and (d2) were added to provide the spatial distribution for the large-scale MHT (Note that the large-scale component of MHT was calculated as the residual between total and mesoscale spatial patterns of SST and velocities). Despite that the MHT induced by mesoscale eddies is much smaller than the large-scale component, an analogy for the opposite effects between Ekman and geostrophic members is still apparent at the large scale, especially in tropical and subtropical regions.

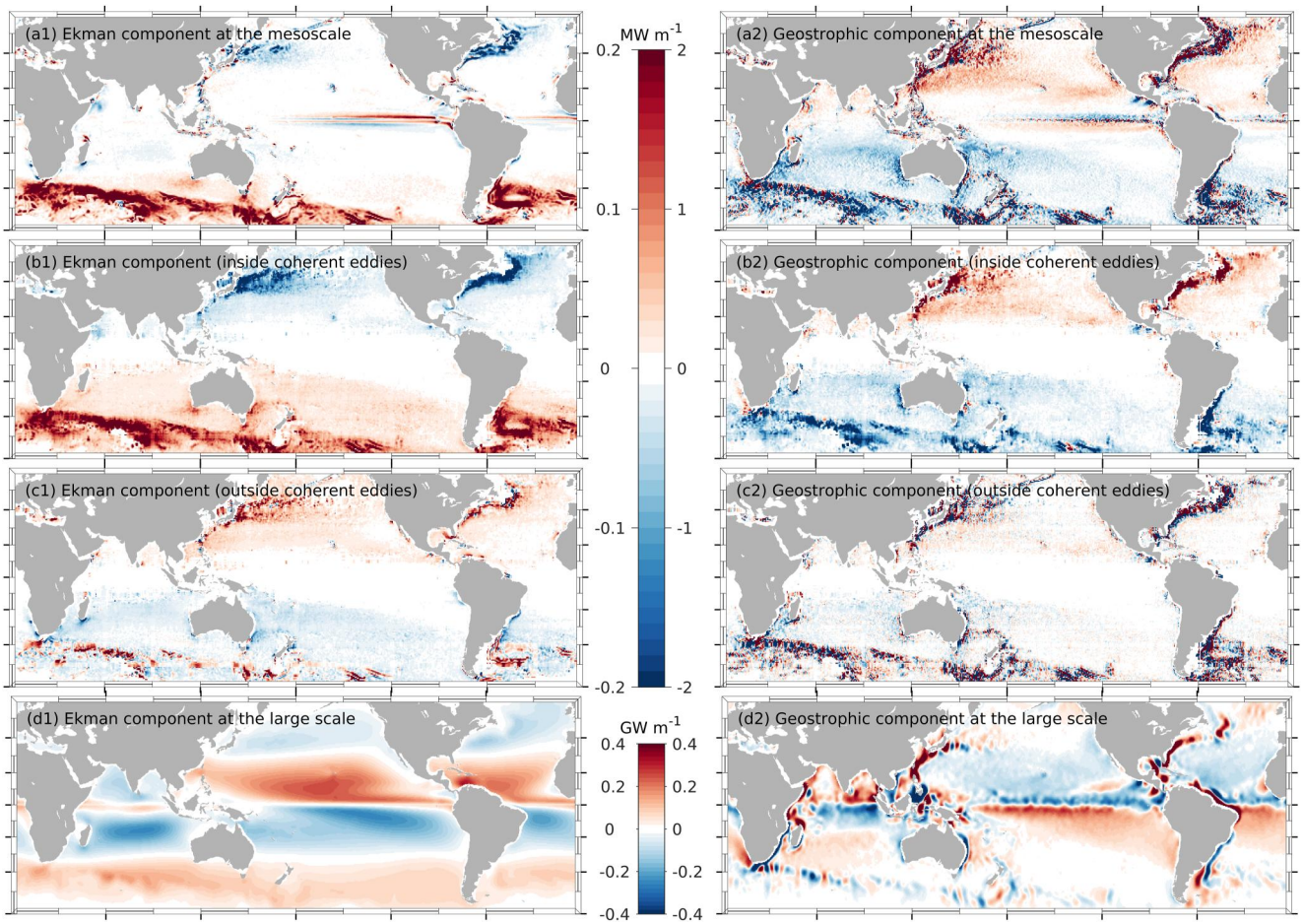

Figure 2. Meridional heat transport (MHT) for the eddy-induced Ekman (left) and geostrophic (right) components. Rows (a–c) respectively display MHT for the total mesoscale signal, inside SSH-SST coherent eddies and outside coherent eddies. Note that the color scale for the Ekman and geostrophic MHT differs by a factor of 10. Panels (d1) and (d2) show the large-scale signal of MHT for comparison with the mesoscale. Positive values indicate the northward movement (1 GW = 1000 MW).

To summarize the spatial distribution of MHT in Figure 2, a schematic of eddy-induced air-sea heat flux (or SST) and its connection with Ekman and geostrophic velocities is provided in Figure 3. The only reason for the appearance of geostrophic MHT component is attributed to the distance between the SSH and SST eddy cores so that a geostrophic balance in velocity can still produce net heat transport meridionally. On the other hand, the

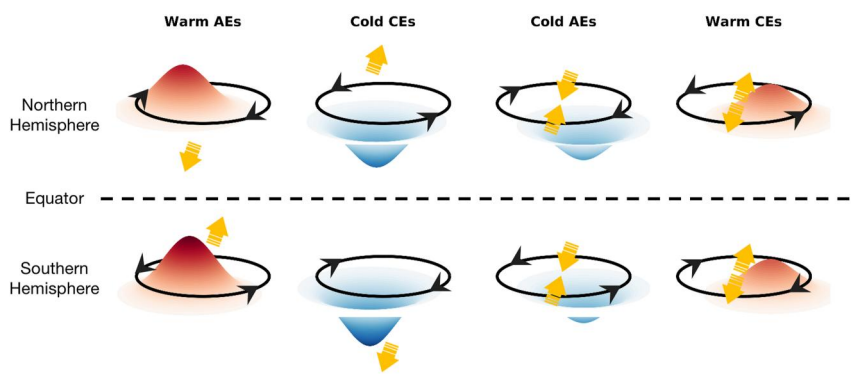

Figure 3. Schematic of SST and velocity anomalies inside SSH-SST coherent and incoherent eddies. Each dome (in red) or basin (in blue) indicates the SST or heat anomaly with some shift of distance from the eddy circulation core. Such pattern of shifts was summarized from the composite analyses of all eddies. Black circles with arrows draw the geostrophic balance of each eddy, while the yellow arrows show the Ekman velocity at the mesoscale.

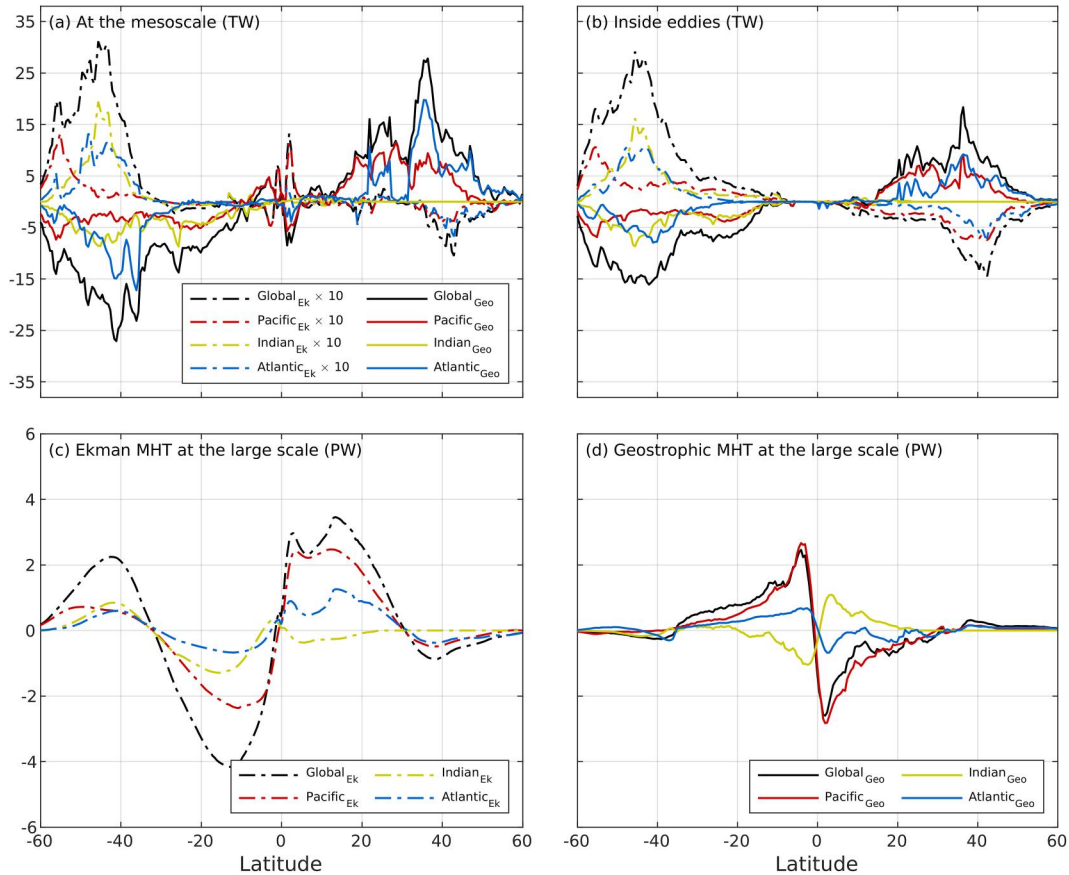

Figure 4. Zonal integration of meridional heat transport (MHT): (a) at the mesoscale; (b) inside mesoscale eddies (including both SSH-SST coherent and incoherent eddies); (c) at the large scale for the Ekman component; (d) at the large scale for the geostrophic component. The legend in (a) also applies to (b). For panels (a) and (b), the magnitude of Ekman components was multiplied by 10 in order to compare the Ekman and geostrophic components in the same plot. The units for (a) and (b) are TW, and units for (c) and (d) are PW (1 PW = 1000 TW).

Ekman dynamics of mesoscale eddies is typically determined by the shear of wind field or the relative vorticity of eddies (e.g., eddy killing effect (Rai et al., 2021) and nonlinear Ekman-layer response to the wind stress (Chen et al., 2021)) while the SST-induced thermal feedback is considered secondary in determining Ekman velocities (Gaube et al., 2015). In the Northern Hemisphere, warm signals of AE migrate toward the equator while cold signals of CE move apart from the equator, both of which produce a negative heat transport (i.e., in the direction toward the equator). A similar combination of the Southern Hemisphere SSH-SST coherent eddies appears to be positive. For SSH-SST incoherent eddies, it is of interest to underline that the meridional components of Ekman velocity anomaly have opposite signs for the northern and southern halves within each eddy contour (Figure S1 in Supporting Information S1). As a result, the Ekman component of MHT for incoherent eddies is also contingent on the meridional distance between the SST- and SSH-determined eddy cores.

The zonal integration of MHT according to Figure 2 leads to Figure 4. A comparison between (a) and (b) shows that eddies as isolated vortices play an essential role in meridional heat transport at the mesoscale. Located near 40° in both hemispheres, the maximums of mesoscale MHT in (a) can approach 3.1 TW for the Ekman component and 26 TW for the geostrophic component. The large-scale MHT shown in (c) and (d) suggests that the total mesoscale signal of MHT is much smaller in comparison. Consistent with previous studies (Jayne & Marotzke, 2002), the large-scale geostrophic MHT dominates the tropical region as shown in (d), whereas the Ekman component switches the sign from subpolar to subtropical regions.

Focused on the mesoscale in Figures 4a and 4b, the Atlantic Ocean (blue lines in the figure) predominates the global pattern for both the geostrophic and Ekman constituents at the mesoscale. In the Southern Hemisphere, the

Ekman component prevails in the Indian Ocean subtropics, which implies that the intensities of SST and wind stress anomalies are both large there. By contrast, the Pacific Ocean is trivial for the Southern Hemisphere MHT at low latitudes, but produces the largest proportion for latitudes higher than 55°S. In the Northern Hemisphere, the geostrophic component of Pacific Ocean induces the largest percentage of MHT at the subtropics, while Atlantic Ocean is more important at polar and subpolar regions.

4. Conclusions and Discussions

The goal of this study is to quantify the near-surface horizontal heat transport at the ocean mesoscale. Such process in the equivalent context of the large scale was often accomplished by diagnosing the meridional overturning circulation, either by direct measurements in depth or indirect deductions from air-sea heat exchanges. Here, we have shown that a more quantitative picture can be inferred from a combination of sea surface thermal and dynamical observations of mesoscale features. To our knowledge, this is the first study that investigates the mesoscale heat transport at the sea surface, in terms of the inconsistency between mesoscale eddy's temperature and velocity characteristics.

With an attempt to retain air-sea variables at the corresponding mesoscale, a filtering window in both space and time was first applied to the original OAFlux2 data set that synthesizes several satellite sensors to generate a more accurate detection of SST, turbulent heat flux, and current velocity fields etc. Second, the META3.2 eddy atlas was included to provide information of isolated eddies as dynamical features. Subsequently, an analysis by compositing mesoscale eddies together led to the concept of SSH-SST coherent (warm AEs and cold CEs) and incoherent (warm CEs and cold AEs) eddies, which were distinguished as whether the eddy's thermal and dynamic structures are consistent in the traditional context. Globally speaking, we find that SSH-SST coherent eddies dominate the mesoscale MHT, albeit a higher proportion of incoherent eddies in specific regions (e.g., the percentage of each eddy type is summarized in Figure 1).

An additional comparison between meridional heat transport by the Ekman flow and geostrophic circulation associated with mesoscale eddies highlights the importance of the distance between eddy's SST- and SSH-determined centers. Without such distance, the approximately geostrophic balance of eddies hardly produces any net transport of heat toward the pole or equator. Overall, the geostrophic MHT is 10 times larger than that originated from the Ekman dynamics. In terms of division into ocean basins, the Atlantic Ocean dominates geostrophic MHT in both hemispheres, while the Indian Ocean plays a leading role in the Southern Hemisphere Ekman heat transport.

In summary, though the mesoscale MHT as defined herein is not comparable to the large scale, mesoscale MHT can still reach 26 TW as the geostrophic component and 3 TW as the Ekman component. Further analyses and investigations could incorporate several extensions to this study:

1. A comparison to the 3D perspective of heat transport calculation could be included. This will be more feasible for numerical studies that consider more complicated equations of state which are capable of producing SSH-SST incoherent eddies.
2. In this study, the thickness of surface layer is uniform for the calculation of MHT. However, previous studies have shown that the surface layer depth is highly dependent on eddy's activities (Gaube et al., 2019), since mesoscale eddies commonly display surface thermal anomalies in contrast to the background water properties under the same atmospheric conditions. A time- or space-varying surface layer thickness might be taken into consideration for a more accurate estimate of MHT.
3. A detailed analysis of depth-dependent structures of mesoscale eddies is necessary for better understanding of SSH-SST incoherent eddies.

Data Availability Statement

The high-resolution air-sea turbulent heat fluxes and related variables are provided by the WHOI OAFlux project (Yu, 2019). The radiation data are provided by CERES (Doelling et al., 2016). The mesoscale eddy atlas and related geostrophic velocity are provided by AVISO (Pegliasco et al., 2022) and CMEMS (Copernicus Marine Service, 2023).

Acknowledgments
The authors are sincerely grateful for funding supports from NASA Making Earth System Data Records for Use in Research Environments (MEaSUREs) Program, Grant 80NSSC18M0079, and NOAA Ocean Monitoring and Observing (GOMO) program, Grant NA19OAR4320074. We also thank the two anonymous reviewers for their constructive comments.

References

Bashmachnikov, I. L., Raj, R. P., Golubkin, P., & Kozlov, I. E. (2023). Heat transport by mesoscale eddies in the Norwegian and Greenland seas. *Journal of Geophysical Research: Oceans*, *128*(2), e2022JC018987. https://doi.org/10.1029/2022JC018987

Bryden, H. L., Roemmich, D. H., & Church, J. A. (1991). Ocean heat transport across 24°N in the pacific. *Deep-Sea Research, Part A: Oceanographic Research Papers*, *38*(3), 297–324. https://doi.org/10.1016/0198-0149(91)90070-V

Chassignet, E. P., & Cushman-Roisin, B. (1991). On the influence of a lower layer on the propagation of nonlinear oceanic eddies. *Journal of Physical Oceanography*, *21*(7), 939–957. https://doi.org/10.1175/1520-0485(1991)021⟨0939:OTIOAL⟩2.0.CO;2

Chelton, D. B., Schlax, M. G., & Samelson, R. M. (2011). Global observations of nonlinear mesoscale eddies. *Progress in Oceanography*, *91*(2), 167–216. https://doi.org/10.1016/j.pocean.2011.01.002

Chen, Y., Straub, D., & Nadeau, L.-P. (2021). Interaction of nonlinear Ekman pumping, near-inertial oscillations, and geostrophic turbulence in an idealized coupled model. *Journal of Physical Oceanography*, *51*(3), 975–987. https://doi.org/10.1175/JPO-D-20-0268.1

Cooley, S., Schoeman, D., Bopp, L., Boyd, P., Donner, S., Ghebrehiwet, D., et al. (2022). Ocean and coastal ecosystems and their services. In H. O. Pörtner, et al. (Eds.), *Climate change 2022: Impacts, adaptation and vulnerability. contribution of working group ii to the sixth assessment report of the intergovernmental panel on climate change* (pp. 379–550). Cambridge University Press. https://doi.org/10.1017/9781009325844.005

Copernicus Marine Service (2023). Global ocean gridded l4 sea surface heights and derived variables reprocessed (1993–ongoing) [Dataset]. Copernicus. https://doi.org/10.48670/moi-00148

Cushman-Roisin, B., Tang, B., & Chassignet, E. P. (1990). Westward motion of mesoscale eddies. *Journal of Physical Oceanography*, *20*(5), 758–768. https://doi.org/10.1175/1520-0485(1990)020⟨0758:WMOME⟩2.0.CO;2

Czaja, A., & Marshall, J. (2006). The partitioning of poleward heat transport between the atmosphere and ocean. *Journal of the Atmospheric Sciences*, *63*(5), 1498–1511. https://doi.org/10.1175/JAS3695.1

Delman, A., & Lee, T. (2021). Global contributions of mesoscale dynamics to meridional heat transport. *Ocean Science*, *17*(4), 1031–1052. https://doi.org/10.5194/os-17-1031-2021

Doelling, D. R., Sun, M., Nguyen, L. T., Nordeen, M. L., Haney, C. O., Keyes, D. F., & Mlynczak, P. E. (2016). Advances in geostationary-derived longwave fluxes for the CERES synoptic (SYN1deg) product. *Journal of Atmospheric and Oceanic Technology*, *33*(3), 503–521. https://doi.org/10.1175/JTECH-D-15-0147.1

Fairall, C. W., Bradley, E. F., Hare, J. E., Grachev, A. A., & Edson, J. B. (2003). Bulk parameterization of air–sea fluxes: Updates and verification for the coare algorithm. *Journal of Climate*, *16*(4), 571–591. https://doi.org/10.1175/1520-0442(2003)016⟨0571:BPOASF⟩2.0.CO;2

Ferrari, R., & Ferreira, D. (2011). What processes drive the ocean heat transport? *Ocean Modelling*, *38*(3), 171–186. https://doi.org/10.1016/j.ocemod.2011.02.013

Gaube, P., Chelton, D. B., Samelson, R. M., Schlax, M. G., & O'Neill, L. W. (2015). Satellite observations of mesoscale eddy-induced Ekman pumping. *Journal of Physical Oceanography*, *45*(1), 104–132. https://doi.org/10.1175/JPO-D-14-0032.1

Gaube, P., McGillicuddy, D. J., Jr., & Moulin, A. J. (2019). Mesoscale eddies modulate mixed layer depth globally. *Geophysical Research Letters*, *46*(3), 1505–1512. https://doi.org/10.1029/2018GL080006

Hausmann, U., & Czaja, A. (2012). The observed signature of mesoscale eddies in sea surface temperature and the associated heat transport. *Deep Sea Research Part I: Oceanographic Research Papers*, *70*, 60–72. https://doi.org/10.1016/j.dsr.2012.08.005

Itoh, S., & Yasuda, I. (2010). Water mass structure of warm and cold anticyclonic eddies in the western boundary region of the subarctic north pacific. *Journal of Physical Oceanography*, *40*(12), 2624–2642. https://doi.org/10.1175/2010JPO4475.1

Jayne, S. R., & Marotzke, J. (2002). The oceanic eddy heat transport. *Journal of Physical Oceanography*, *32*(12), 3328–3345. https://doi.org/10.1175/1520-0485(2002)032⟨3328:TOEHT⟩2.0.CO;2

Johns, W. E., Baringer, M. O., Beal, L. M., Cunningham, S. A., Kanzow, T., Bryden, H. L., et al. (2011). Continuous, array-based estimates of Atlantic Ocean heat transport at 26.5°N. *Journal of Climate*, *24*(10), 2429–2449. https://doi.org/10.1175/2010JCLI3997.1

Keeling, R. F., Körtzinger, A., & Gruber, N. (2010). Ocean deoxygenation in a warming world. *Annual Review of Marine Science*, *2*(1), 199–229. https://doi.org/10.1146/annurev.marine.010908.163855

Liu, Y., Yu, L., & Chen, G. (2020). Characterization of sea surface temperature and air-sea heat flux anomalies associated with mesoscale eddies in the South China Sea. *Journal of Geophysical Research: Oceans*, *125*(4), e2019JC015470. https://doi.org/10.1029/2019JC015470

Madakumbura, G. D., Thackeray, C. W., Norris, J., Goldenson, N., & Hall, A. (2021). Anthropogenic influence on extreme precipitation over global land areas seen in multiple observational datasets. *Nature Communications*, *12*(1), 3944. https://doi.org/10.1038/s41467-021-24262-x

Marzeion, B., Cogley, J. G., Richter, K., & Parkes, D. (2014). Attribution of global glacier mass loss to anthropogenic and natural causes. *Science*, *345*(6199), 919–921. https://doi.org/10.1126/science.1254702

Melnichenko, O., Amores, A., Maximenko, N., Hacker, P., & Potemra, J. (2017). Signature of mesoscale eddies in satellite sea surface salinity data. *Journal of Geophysical Research: Oceans*, *122*(2), 1416–1424. https://doi.org/10.1002/2016JC012420

Morrow, R., Birol, F., Griffin, D., & Sudre, J. (2004). Divergent pathways of cyclonic and anti-cyclonic ocean eddies. *Geophysical Research Letters*, *31*(24), L24311. https://doi.org/10.1029/2004GL020974

Moschos, E., Barboni, A., & Stegner, A. (2022). Why do inverse eddy surface temperature anomalies emerge? The case of the Mediterranean Sea. *Remote Sensing*, *14*(15), 3807. https://doi.org/10.3390/rs14153807

Ni, Q., Zhai, X., Jiang, X., & Chen, D. (2021). Abundant cold anticyclonic eddies and warm cyclonic eddies in the global ocean. *Journal of Physical Oceanography*, *51*(9), 2793–2806. https://doi.org/10.1175/JPO-D-21-0010.1

Nurser, A. J. G., & Lee, M.-M. (2004). Isopycnal averaging at constant height. Part I: The formulation and a case study. *Journal of Physical Oceanography*, *34*(12), 2721–2739. https://doi.org/10.1175/JPO2649.1

Pegliasco, C., Busché, C., & Faugère, Y. (2022). Mesoscale eddy trajectory atlas meta3.2 delayed-time all satellites. *CNES*. https://doi.org/10.24400/527896/A01-2022.005

Rai, S., Hecht, M., Maltrud, M., & Aluie, H. (2021). Scale of oceanic eddy killing by wind from global satellite observations. *Science Advances*, *7*(28), eabf4920. https://doi.org/10.1126/sciadv.abf4920

Roemmich, D., & Wunsch, C. (1985). Two transatlantic sections: Meridional circulation and heat flux in the subtropical North Atlantic Ocean. *Deep Sea Research Part A. Oceanographic Research Papers*, *32*(6), 619–664. https://doi.org/10.1016/0198-0149(85)90070-6

Stern, M. E. (1965). Interaction of a uniform wind stress with a geostrophic vortex. *Deep-Sea Research and Oceanographic Abstracts*, *12*(3), 355–367. https://doi.org/10.1016/0011-7471(65)90007-0

Sun, B., Liu, C., & Wang, F. (2019). Global meridional eddy heat transport inferred from Argo and altimetry observations. *Scientific Reports*, *9*(1), 1345. https://doi.org/10.1038/s41598-018-38069-2

Sun, W., An, M., Liu, J., Liu, J., Yang, J., Tan, W., et al. (2022). Comparative analysis of four types of mesoscale eddies in the kuroshio-oyashio extension region. *Frontiers in Marine Science*, *9*. https://doi.org/10.3389/fmars.2022.984244

Talley, L. D. (2003). Shallow, intermediate, and deep overturning components of the global heat budget. *Journal of Physical Oceanography*, *33*(3), 530–560. https://doi.org/10.1175/1520-0485(2003)033⟨0530:SIADOC⟩2.0.CO;2

Trenberth, K. E., & Caron, J. M. (2001). Estimates of meridional atmosphere and ocean heat transports. *Journal of Climate*, *14*(16), 3433–3443. https://doi.org/10.1175/1520-0442(2001)014⟨3433:EOMAAO⟩2.0.CO;2

Trenberth, K. E., & Fasullo, J. T. (2017). Atlantic meridional heat transports computed from balancing earth's energy locally. *Geophysical Research Letters*, *44*(4), 1919–1927. https://doi.org/10.1002/2016GL072475

Villas Bôas, A. B., Sato, O. T., Chaigneau, A., & Castelão, G. P. (2015). The signature of mesoscale eddies on the air-sea turbulent heat fluxes in the South Atlantic Ocean. *Geophysical Research Letters*, *42*(6), 1856–1862. https://doi.org/10.1002/2015GL063105

Warren, B. A. (1999). Approximating the energy transport across oceanic sections. *Journal of Geophysical Research*, *104*(C4), 7915–7919. https://doi.org/10.1029/1998JC900089

Yu, L. (2019). Global air–sea fluxes of heat, fresh water, and momentum: Energy budget closure and unanswered questions. *Annual Review of Marine Science*, *11*(1), 227–248. https://doi.org/10.1146/annurev-marine-010816-060704

Yu, L., & Jin, X. (2014a). Confidence and sensitivity study of the oaflux multisensor synthesis of the global ocean surface vector wind from 1987 onward. *Journal of Geophysical Research: Oceans*, *119*(10), 6842–6862. https://doi.org/10.1002/2014JC010194

Yu, L., & Jin, X. (2014b). Insights on the OAFlux ocean surface vector wind analysis merged from scatterometers and passive microwave radiometers (1987 onward). *Journal of Geophysical Research: Oceans*, *119*(8), 5244–5269. https://doi.org/10.1002/2013JC009648

Yu, L., & Jin, X. (2018). A regime-dependent retrieval algorithm for near-surface air temperature and specific humidity from multi-microwave sensors. *Remote Sensing of Environment*, *215*, 199–216. https://doi.org/10.1016/j.rse.2018.06.001

Zickfeld, K., Solomon, S., & Gilford, D. M. (2017). Centuries of thermal sea-level rise due to anthropogenic emissions of short-lived greenhouse gases. *Proceedings of the National Academy of Sciences*, *114*(4), 657–662. https://doi.org/10.1073/pnas.1612066114